Spatio-temporal elasticity patterns in extracellular matrix during Hydra morphogenesis

Mariam Veschgini[a], Hendrik O. Petersen[b], Wasim Abuillan[a], Fernanda F. Rossetti[a], Suat Özbek[b], Manfred Burghammer[c], Thomas W. Holstein[b,*], Motomu Tanaka[a,d,*].

[a] Physical Chemistry of Biosystems, Institute of Physical Chemistry, University of Heidelberg, Im Neuenheimer Feld 253, D-69120 Heidelberg, Germany
[b] Centre for Organismal Studies, Department of Molecular Evolution and Genomics, University of Heidelberg, D-69120 Heidelberg, Germany
[c] European Synchrotron Radiation Facility, 71 Avenue des Martyrs, F-38000 Grenoble, France
[d] Institute for Integrated Cell-Material Sciences, Kyoto University, Kyoto 606-8501, Japan
* Corresponding authors: tanaka@uni-heidelberg.de and thomas.holstein@cos.uni-heidelberg.de

Keywords: extracellular matrix, Hydra, nano-focused GISAXS, elasticity pattern, proteomics

Abstract

Although mounting *in vitro* studies suggest a critical impact of structural and mechanical properties of the surrounding microenvironment on stem cell maintenance and differentiation, little is known about how extracellular matrix (ECM) remodeling co-ordinates stem cell behavior *in vivo*. In this study we used the native ECM (mesoglea) of the freshwater polyp Hydra and determined the mesoscopic ECM structure by grazing-incidence small-angle X-ray scattering using a nano-focused beam. We found that the packing of Hydra collagen fibrils is comparable to that in vertebrates. It is also highly anisotropic with respect to the main (oral-aboral) body axis explaining the very dynamic contraction and extension behavior of a Hydra polyp. We monitored the spatio-temporal evolution of ECM mechanics *ex vivo* during Hydra maturation by mapping the elastic modulus of Hydra mesoglea along the main body axis before and after the budding with aid of nano-indentation. The extracted characteristic elasticity patterns implied that freshly detached polyps bear a mesoglea of uniform elasticity. By time, the mesoglea becomes softer in the upper gastric region but stiffer in the middle and lower region, where new buds emerge. The complementary proteome analysis demonstrated that the observed changes in mechanical patterns are correlated with the activity of proteases. Our data are consistent with a model according to which regions of high ECM stiffness facilitate stem cell activity in a given tissue.

Introduction

The extracellular matrix (ECM) is a unique component that regulates the homeostasis of animal tissue, supporting the structural integrity and cell functions (1). Recent *in vitro* studies suggested that the mechanical properties of ECM strongly affect stem cell migration, proliferation and differentiation (2-5). Moreover, an *ex vivo* study on human lung tissues implied that abnormal ECM stiffness is correlated with pulmonary fibrosis (6). Recently, we found that human mesenchymal stem cells decide their fate in response to dynamic changes in the micromechanical environments (7). Therefore, stem cells might sense a variety of physical cues within their microenvironment (8-9), including the stiffness of the ECM. However, in living organisms only little is understood about the relationship between ECM mechanics and tissue morphogenesis.

In this paper, we investigated the correlation between biophysical properties and functions of native ECM of the ancient fresh water polyp Hydra, which is a paradigm for an almost unlimited regeneration capability. Compared to 'higher' animals, it has a simple sack-like body plan with a body wall composed of an ECM, called mesoglea, which separates two cell layers; an outer ectoderm and an inner endoderm. The cells consist of three stem cell lineages undergoing continuous cell division in the body column: endo- and ectodermal epithelial-muscular cells and interstitial stem cells (10). The molecular composition of Hydra's mesoglea exhibits a high degree of similarity to vertebrate ECM, containing heparan sulfate proteoglycans, laminin and fibronectin-like molecules as well as fibrillar (type I and II) and non-fibrillar (type IV) collagens (11). Hydra ECM combines two major ECM functions that are separated in higher animals, i.e. mechanical integrity guaranteed by collagen fibers in connective tissues, and cell-cell communications mediated by basal lamina (11). To accommodate both functions, Hydra mesoglea forms a tri-laminar structure: two thin sub-epithelial zones based on collagen type IV and laminin sandwich a central fibrous zone, the

interstitial matrix consisting of a grid of collagen type I fibrils (Hcol-I) (12-13). However, although the compositions of mesoglea are comparable to those of vertebrates (14), there has been no quantitative comparison of the supramolecular organization between Hydra and vertebrates. To gain the first insight, we performed grazing-incidence small-angle X-ray scattering of Hydra mesoglea by focusing a monochromatic synchrotron X-ray beam to the diameter of 200 nm. We unraveled that the fibrillar proteins in Hydra mesoglea possess packing lattice parameters comparable to those in vertebrates. Moreover, they exhibit a clear anisotropy with respect to the oral-aboral body axis (OA-axis).

The mesoglea plays an important role in Hydra morphogenesis (15-17). It is dynamically remodeled during growth and differentiation of Hydra and a significant change in fiber network of mesoglea along the body column of Hydras was observed during budding (18-19), Hydra's form of asexual reproduction. The mesoglea of buds was described to be thinner than that of the mother polyp (20) suggesting some correlation between structure and mechanics of the mesoglea during morphogenesis. In a study on jellyfish mesoglea it was proposed that aging causes an increase in the overall elastic modulus of the ECM (21). However, the jellyfish mesoglea represents a bulky structure enabling the animals buoyancy in the water column (22). Thus, a less derived ancient model is needed for understanding the basic functions of the ECM in tissue and stem cell homeostasis. Since there has been no quantitative study on the spatial pattern in mesoglea mechanics during growth and development in Hydra, we measured the spatio-temporal changes of mesoglea strength along the polyp's OA-axis using nano-indentation with an atomic force microscope (AFM). The indentation of mesoglea samples isolated at different ages of buds and polyps demonstrated that the break of the radial body symmetry in Hydra during budding is accompanied by coordinated softening of the upper gastric and stiffening of the budding region. Furthermore, we compared the elasticity patterns with the protease profiles in a focused proteome analysis implying significant changes in protease expression patterns along the OA-axis. By analyzing also transgenic strains and animals with an activated Wnt pathway we found that regions with high stiffness of the ECM were correlated with regions of high stem cell activity, but not an increased bending of the tissue.

Results

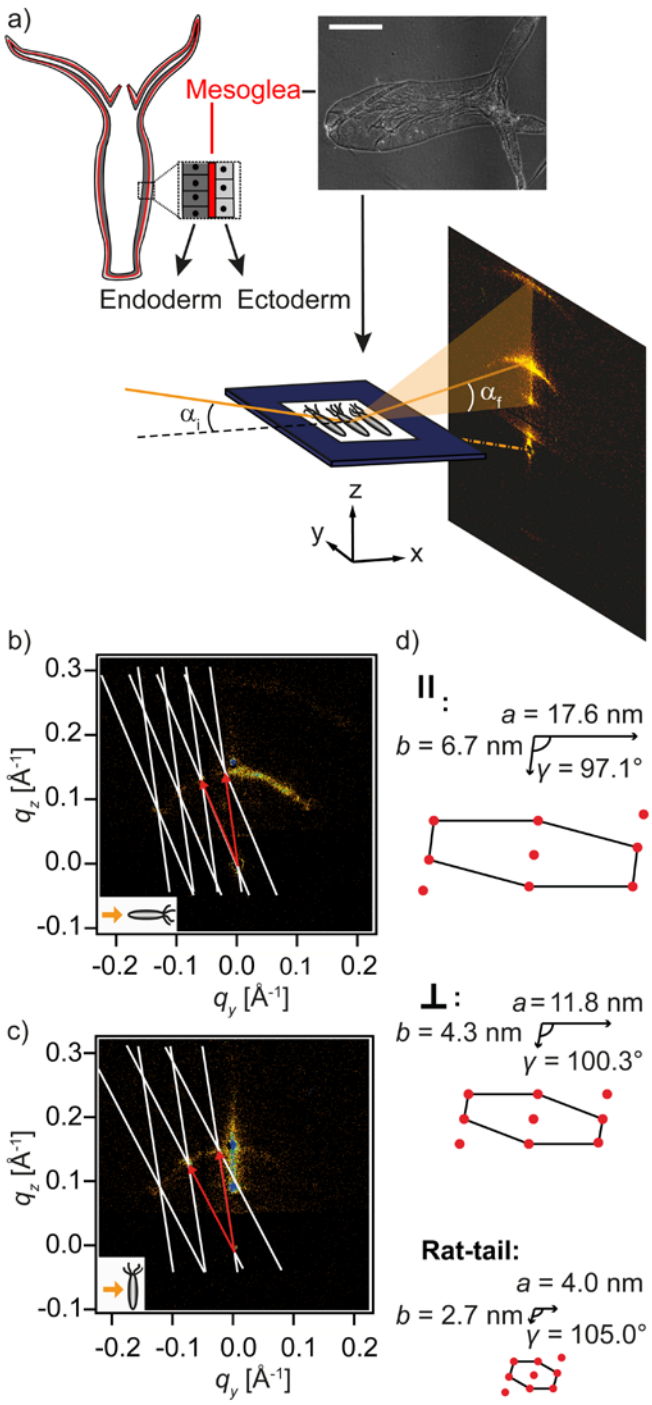

Figure 1. Nano-focused GISAXS of isolated Hydra mesoglea. (a) Top left: schematic illustration of Hydra body structure. Mesoglea was isolated by freeze-thawing. Top right: phase contrast microscopy image of isolated mesoglea. Scale bar corresponds to 500 µm. Bottom: experimental setup of nano-GISAXS. Isolated mesoglea was placed on a silicon nitride window and illuminated by an X-ray beam at a grazing incidence angle α_i. Scattering patterns obtained with the beam parallel (b) and perpendicular (c) to the major body axis (see inset yellow arrow). The white grid represents the reciprocal lattice, while lattice vectors are indicated in red. (d) Lattice parameters in real space (a, b, γ) calculated from the direction

parallel (top) and perpendicular (middle) to the major body axis. For comparison, the lattice parameters from the reference sample (collagen type I from rat tail tendon) (23) are presented (bottom).

Mesoscopic structure of the mesoglea. To compare the mesoscopic structure of the mesoglea with those of vertebrates, we performed a nano-GISAXS analysis. Figure 1a schematically illustrates the experimental setup and sample geometry of nano-GISAXS. The isolated mesoglea (see Materials and Methods) was deposited on silicon nitride membranes. A monochromatic, nano-focused beam illuminated the sample at an incident angle α_i = 0.46°, which is beyond the critical angle of total external reflection (α_c = 0.14°). Nano-GISAXS patterns obtained from the directions parallel and perpendicular to the OA-axis of mesoglea are presented in Figures 1b and 1c, respectively.

Several patterns showed that one or more arcs were arranged concentrically around the direct beam, accompanied by additional satellite peaks positioned on the arcs (Figure1d). The white grid overlaid on each pattern represents the reconstructed reciprocal lattice. The obtained lattice patterns clearly indicate the presence of anisotropically arranged rod-like objects that are aligned parallel to the substrate surface, which can be attributed to type I collagen fibers. The real space lattice parameters (a, b, γ) calculated from the GISAXS patterns parallel and perpendicular to the Hydra body axis, are presented in the top and middle panels of Figure 1d, respectively. The lattice parameters of the mesoglea parallel to the OA-axis are $a_{||}$ = (17.6 ± 3.6) nm, $b_{||}$ = (6.7 ± 0.8) nm and $\gamma_{||}$ = (97.1 ± 2.4)°, while those perpendicular to the body axis are $a_{\perp}$ = (11.8 ± 0.5) nm, $b_{\perp}$ = (4.3 ± 0.4) nm and $\gamma_{\perp}$ = (100.3 ± 9.3)°. Our nano-GISAXS results quantitatively demonstrate for the first time that the fibrillar proteins of Hydra mesoglea are comparable to those of vertebrates (i.e. rat tail collagen type I (23), Figure 1d, bottom). The results further show that the fibrillar proteins in Hydra mesoglea take an anisotropic packing order with respect to OA-axis of the animal. A loose, distorted packing of Hydra collagen seems to support the highly dynamic extension and contraction of Hydra along the body axis (13, 24).

Mechanical properties of the mesoglea. In order to probe the spatial distribution of mesoglea mechanics, we

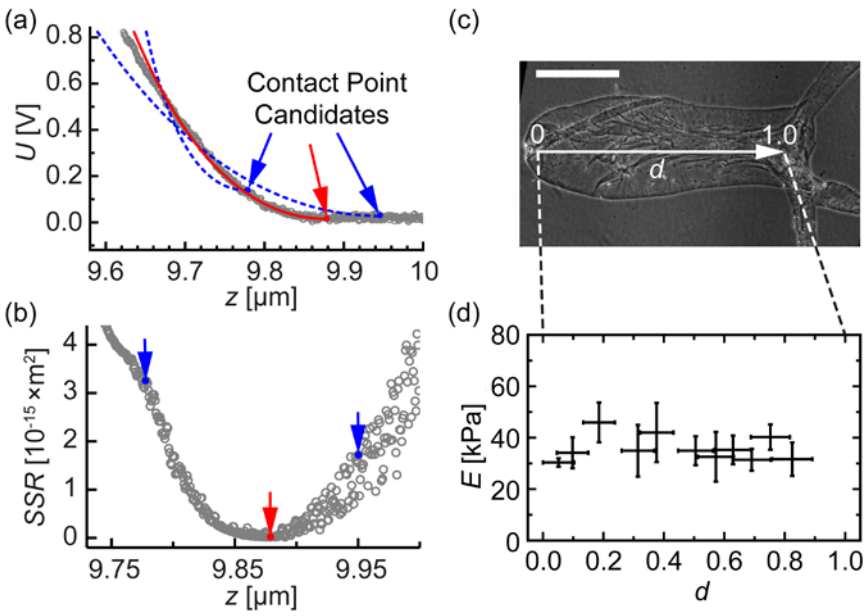

Figure 2. Derivation of mesoglea elasticity map. (a) Optimization of the data analysis. The measured data points (deflection voltage vs. the tip position, gray circles) are fitted by moving the contact points along the data set. Three contact points (indicated by arrows) are presented together with the corresponding fits (dashed and solid lines). The best fitted model (solid red line) implies the Young's modulus of E = 29.7 kPa for position d = 0.57 in part d. (b) Evolution of the mean sum of square residuals (SSR) during the marching of the contact point candidate over data points in the vicinity of the onset point. Blue and red points correspond to the points indicated in b. The red contact point candidate yields the minimum SSR. (c) Phase contrast microscopy image of an isolated mesoglea. Scale bar corresponds to 500 µm (d) The "elasticity map" of a mesoglea vs. d, which is the relative distance of indentation position from "mesoglea foot" as indicated by the white arrow in part c. Error bars for E correspond to the standard deviation out of 8 independent measurements.

mapped the elasticity of mesoglea along the OA-axis with the aid of AFM nano-indentation. A force-distance curve measured on mesoglea is exemplified in Figure 2a (gray circles). The Bilodeau model (25) was used to calculate the Young's modulus. The tip-sample contact point (z_0, d_0), which is crucial for the analysis of soft materials, was carefully optimized by a sequential search (26-27). The contact point candidate was marched over the points near the onset point (Figure 2a), and Young's modulus was extracted from the least-square fit model. As illustrated in Figure 2b, the goodness of the fit decreases by moving further from the optimal point (red point in Figure 2a and 2b). Figure 2c shows a mesoglea extracted from a freshly detached Hydra, and the corresponding elasticity map is shown in Figure 2d. Each data point represents the mean average of up to 8 independent measurements. The indentation positions from mesoglea foot were normalized by the body column length, in order to obtain the relative position d (Figure 2c and d). This enables one to segment different regions along body axis according to d: (i) peduncle region ($0.0 \leq d < 0.1$), (ii) budding region ($0.1 \leq d \leq 0.3$), and (iii) upper gastric region ($0.6 \leq d \leq 1.0$).

Utilizing the segmentation described above, the "elasticity maps" extracted from different animals could be classified into three main characteristic phenotypes: Type A, characterized by uniform elastic moduli along the entire body column with $\langle E \rangle$ = 40 - 90 kPa (Figure 3b). Type B with high elastic moduli in the lower body ($\langle E \rangle \leq 120$ kPa) and low values ($\langle E \rangle \geq 15$ kPa) in the upper body (Figure 3c), and the related type C with a lower elasticity ($\langle E \rangle \geq 40$ kPa) in the peduncle (Figure 3d). A schematic overlay of the three main elasticity patterns out of 9 samples is presented in Figure 3f. As described in SI Materials and Methods, the elastic moduli were normalized by those of the budding region to classify the elasticity patterns. Based on these criteria, 66% of measured elasticity patterns could be categorized as type A, 18% as type B and 13% as type C (n = 38).

Developmental stage and mesoglea mechanics. In the next step, the mesoglea mechanics was investigated by sorting the elasticity patterns as a function of Hydra's age and developmental stage, focusing on: freshly detached buds (t = 0 d), polyps at the ages of t = 2 d and 3 d. The characteristic time window of 4 d was chosen in order to focus on the transition from newly detached buds towards budding animals. Polyps freshly detached from the parent (t = 0 d) showed exclusively type A pattern, i.e. the elasticity of mesoglea was low and uniform along the body axis (n = 5). Later the fraction of type A pattern decreased to 40% and type B and C patterns appeared (n = 5). At t = 3 d, type B and type C became more

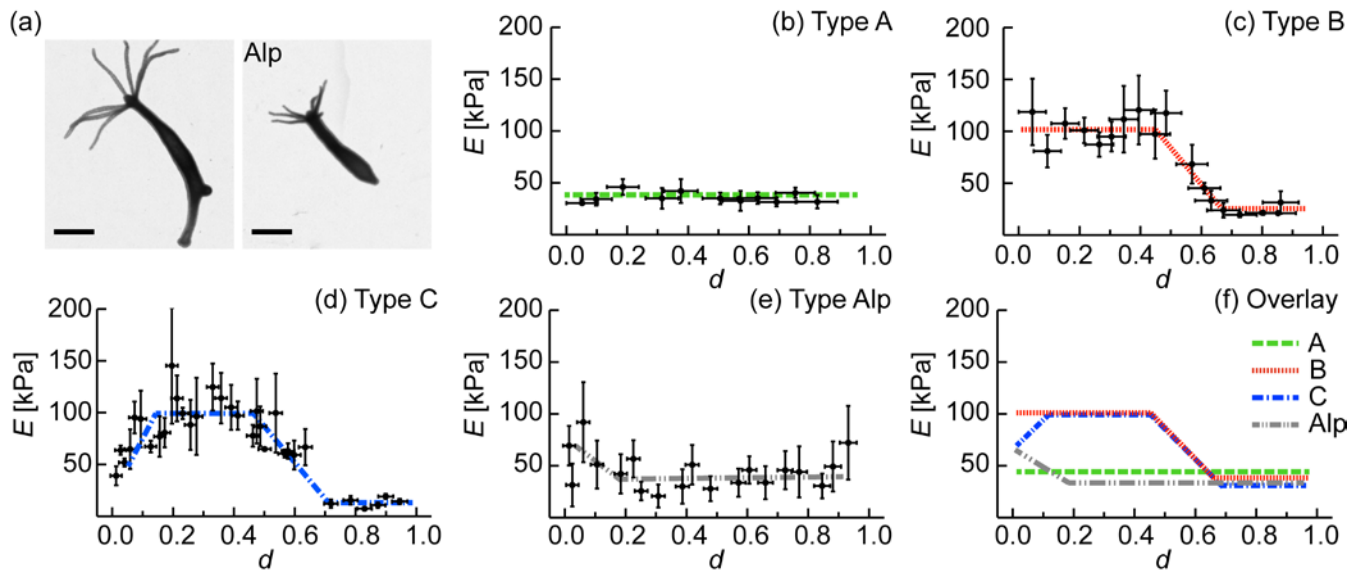

Figure 3. Classification of representative elasticity maps along the main body axis. (a) Light microscopy images of 3 days old hydra magnipapillata with no (left) and 2 days after treatments with alsterpaullone (right). Scale bars correspond to 1 mm. (b) Type A elasticity map, uniform and low elastic modulus along the whole mesoglea; (c) Type B, transition from stiff foot to soft head region; (d) Type C, mesoglea exhibits maximum elastic modulus at d = 0.1 – 0.3. (e) Type Alp. Alsterpaullone treated hydras show a mesoglea with a low elastic modulus in the upper gastric and budding region, which increases slightly towards the foot. (f) Comparison of the absolute levels of four characteristic elasticity patterns.

pronounced, and the fraction of type A pattern decreased to 14% (n = 7). These experimental findings indicate that the maturation of freshly detached buds towards budding animals is strongly correlated with a change in the elasticity patterns of the ECM and an increase in the mechanical strength of the matrix in the presumptive budding zone (see Discussion).

Matrix proteases and mesoglea mechanics. Changes in the elasticity could be either due to posttranscriptional modifications of ECM proteins or the differential expression and composition of ECM proteins exhibiting different elastic properties. To analyze how changes in the elasticity of the mesoglea are molecularly regulated, we performed a quantitative proteomic analysis of mesoglea. We compared the protein expression patterns of mesoglea of (a) freshly detached buds as well as (b) the upper gastric region and (c) budding region of old animals (t = 3 d). Internal standards were the isolated mesoglea from SILAC Hydra containing all developmental stages (28) (see Materials and Methods).

Our quantitative analysis revealed that no core members of the mesoglea proteins (11) changed between the three samples. However, four proteins were significantly up-regulated in the mesoglea from freshly detached buds and the upper gastric of 3 days old polyps: Dickkopf-like protein 1 (Dlp-1) (29-30), a GM2-like protein, and two matrix proteases, i.e. a metallo- and an astacin-like protease (Figure 4). Dlp-1 is an extracellular protein known to be gradually expressed along the OA-axis of Hydra. The fact that no ECM core proteins were differentially expressed indicates that it is not the composition of the ECM, but rather a processing and/or modification of the ECM proteins that is responsible for changes in the elasticity of the mesoglea. The two differentially expressed proteases are potential candidates for this mechanism. Both proteases were strongly abundant in (a) mesoglea of freshly detached buds and (b) upper gastric mesoglea of old polyps, while (c) mesoglea of old animals extracted from the isolated budding region had a lower content of the identified ECM proteases. This finding seems to be fully consistent with the elasticity patterns, where we found that mesoglea from the budding regions of old polyps exhibited a remarkable stiffening, as identified by Type B (Figure 3c) and Type C (Figure 3d), implying that the identified matrix proteases are involved in regulating the elasticity patterns of Hydra's mesoglea.

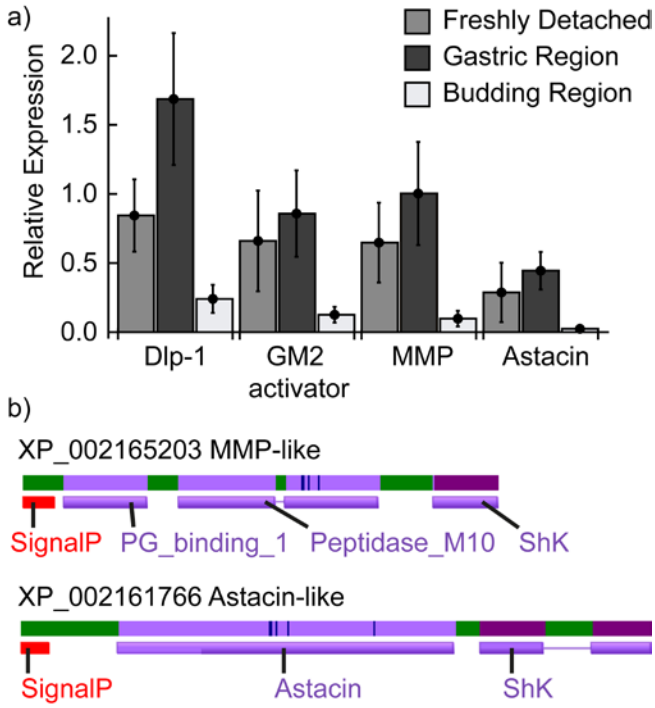

Figure 4. Mesoglea proteome analysis. (A) Protein expression differences in the mesoglea were analyzed between the gastric and budding region of mature animals and between the mesoglea of freshly detached animals. Multiple sample ANNOVA analysis, using a p-value threshold of 0.05, revealed significant expression differences of four proteins between the samples. Among these, two are extracellular proteases (MMP-like and Astacin-like proteases). (C) Domain structure of the differentially expressed proteases.

β-Catenin signaling and mesoglea mechanics. It is well established that Hydra pattern formation strongly depends on Wnt and β-Catenin signaling (31-32). Because matrix metalloproteases are also known to be regulated in a Wnt dependent manner (33-36) we analyzed the effect of Wnt / β-Catenin signaling on the biophysical properties of the mesoglea. We treated Hydra with alsterpaullone (Alp) (SI Materials and Methods), which induces the ectopic activation of Wnt signaling by inhibiting glycogen synthase kinase 3 (GSK3) (37) and induces the formation of ectopic tentacles along the body column after 48 - 72 h. Figure 3 shows that there was a clear difference between Alp-treated and untreated polyps. Alp-treated animals exhibited significant reduction in the elasticity of the mesoglea in contrast to untreated control polyps (Figure 3e). They did not show mesoglea stiffening in the budding region so that the entire body column, including the upper gastric and budding region, exhibited elastic moduli that were comparable to, or even lower than the elasticity of gastric mesoglea of untreated Hydras ($\langle E \rangle \approx 35$ kPa, n = 5). We also analyzed the mesoglea of β-catenin

overexpressing polyps that also have increased levels of tentacle and head structures (38). These polyps were more heterogeneous in the elasticity patterns, likely due to a broader diversity of morphological phenotypes, but in essence it was similar to Alp-type Hydras (SI, Figure S2).

Discussion

The ECM in multicellular organisms is a crucial structure that is serving as a cell substrate and as a medium for the transport of extracellular factors required for coordinated growth and patterning. Ample evidence also suggested that the mesoscopic structural arrangement as well as mechanical properties of ECM support the stem cell maintenance and differentiation (39-41). Hence, dynamic processes such as development and diseases should be accompanied by the dynamic ECM remodeling (1). In this study, we focused on the ECM in Hydra, a model for regenerative biology (28), and we applied nano-GISAXS (42) to gain the mesoscopic structural order of collagen fibers that predominantly govern mesoglea mechanics. AFM nanoindentation further enabled us to extract the spatio-temporal patterns of mesoglea during maturation and asexual budding of a daughter animal, which could be correlated with the protease expression and axial patterning.

Mesoscopic structure of mesoglea. GISAXS measurements with nano-focused beam realize a much smaller beam footprint than a mesoglea, which enables one to gain the mesoscopic structural order of Hydra mesoglea parallel and perpendicular to the OA-axis. Taking this unique advantages, we found that collagen fibers (Hcol-I) take highly asymmetric, distorted hexagonal lattices. The packing of Hcol-I fiber along the body axis was found to be less ordered compared to the one perpendicular to the body axis, which can be attributed to an intrinsic body design of Hydra undergoing significant stretching and contraction along the OA-axis. It is noteworthy that the ordering of Hcol-I fibers in both directions was slightly distorted compared to that of standard samples from vertebrates; rat-tail collagen type I fibers (23, 43-44). Our results seem plausible if one considers the amino acid composition of Hcol-I, which has a lower proline content and lacks typical lysine-crosslinking sites (13). Furthermore, an altered post-translational processing leads to the retention of the N-terminal propeptide-like domains (13), resulting in weaker intermolecular interactions between Hcol-I.

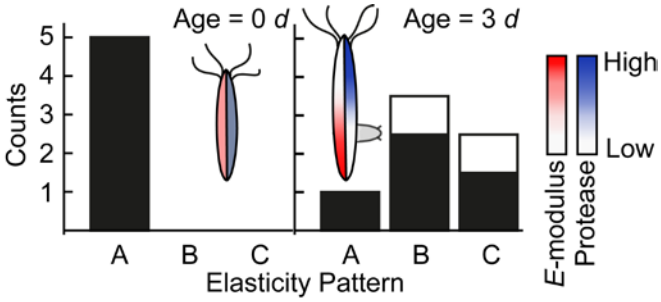

Figure 5. Spatio-temporal remodeling of mesoglea. Young non-budding Hydras show uniformly soft mesogleas (type A) associated with moderate and uniform protease expression level. Temporal changes in protease expression softens mesoglea in gastric region: type B/C pattern (polyps with (black) no apparent buds (white) buds at stage 3 or higher).

Mechanical properties of mesoglea. Although previous studies demonstrated that Hydra's mesoglea is continuously remodeled and displaced towards both ends of the body column (20), there have been no systematic studies on the spatial coordination of this highly dynamic mesoglea mechanics in the context of the growth and development of polyps. In this study, our AFM nano-indentation unraveled striking spatio-temporal patterns of mesoglea elasticity during the maturation of freshly detached daughter animals: after detachment from the parental Hydra, the elasticity maps of the mesoglea from young polyps were all uniform (type A; $\langle E \rangle$ = 40 - 90 kPa), which is in accord with a homogeneous fiber network in young polyps (18-19). The elasticity maps of detached young polyps lose their uniformity in 2 - 3 d, when such polyps form the next generation of buds during asexual reproduction (types B/C). During this maturation time the mesoglea of the lower gastric region – the budding zone – becomes stiffer ($\langle E \rangle$ ~ 100 kPa), while the mesoglea of the upper gastric region becomes softer ($\langle E \rangle$ = 15 ~ 40 kPa).

Matrix proteases and mesoglea mechanics. The underlying molecular mechanisms for the increased stiffness of the mesoglea in the budding zone have not fully been understood yet. Figure 5 summarizes the physical readouts (AFM indentation) and the molecular readouts (proteome analysis) demonstrating the correlation between the spatio-temporal changes in the mechanics and the protease expression levels uncovered in our study. Young polyps (t = 0 d) expressed uniform mesoglea elasticity (Type A) and protease patterns. In contrast, budding Hydras exhibited remarkably high mesoglea stiffness extending to the peduncle and foot (Type B/C). Our proteome analysis indicated that the

transformation in elasticity patterns from type A to type B/C corresponds to changes in the spatial distribution of matrix proteases: it is low in the budding zone and high in the upper gastric region. A high expression level of metalloprotease was also described for the foot (15) explaining the emergence of low stiffness in the peduncle (type C pattern). Therefore, the highly dynamic feature of Hydra mesoglea is developmentally regulated.

β-Catenin signaling and mesoglea mechanics. The stiffening of mesoglea in the budding region suggests a more pronounced cell migration in this zone. During the early stages of budding epithelial cells are displaced with respect to mesoglea into emerging buds, which is different from the normal growth, where the movement of epithelial cells is coupled to that of mesoglea (20). Such a displacement of epithelial cells with respect to mesoglea can also be found in tentacle-base tissue (20). If the increased stiffness of the mesoglea simply reflects the biomechanical constraints of tissue evagination, bud and tentacle forming tissue should exhibit a similar elasticity level. However, when we activated the Wnt pathway by inhibiting GSK3 with Alp and thereby generated animals with multiple tentacles along the entire body column, we got the opposite result. In Alp-treated animals, the mesoglea remained soft ($\langle E \rangle \approx 35$ kPA) along the entire body column. Thus, there is no simple correlation between tissue morphodynamics (e.g. evagination) and the elastic properties of Hydra's ECM.

It is remarkable that the region of high mesoglea stiffness also facilitates high stem cell activity and proliferation. In this region interstitial and epithelial stem cell lineages continuously divide and give rise to several differentiation products, i.e. neuronal cell, gland cells and germ cell precursors (10, 40). The uppermost gastric region and tentacle base tissue with mesoglea of low elastic modulus seem to coincide with the regions of low stem cell activities. We therefore presume that a main function of the differential ECM stiffness in Hydra is to contribute to differential stem cell activity in concert with the various cues of signaling molecules different from Wnt, such as BMP (45-46).

Materials and Methods

Culture. Hydra *magnipapillata* and β-catenin overexpressing Hydras *vulgaris* were cultured in modified Hydra medium (47) (1.0 mM $CaCl_2$, 1.0 mM Tris-HCl, 1.0 mM $NaHCO_3$, 0.1 mM KCl, 0.1 mM $MgCl_2$, pH = 7.4) and kept at (18±0.5)°C. The culture was synchronized as described in SI Materials and Methods. Animals were fed daily with *Artemia* and cleaned a few hours after feeding.

Single mesoglea isolation. 1 day starved Hydras were transferred to a 2 ml test tube with Hydra medium (1 Hydra per tube). Hydra medium was replaced by 1.5 ml of a 0.5% w/v solution of N-Lauroylsarcosine sodium salt in water. The sample was then immersed in liquid nitrogen for 10 min. Frozen Hydras were either used directly or stored at -80 °C. To extract the mesoglea Hydras were transferred to distilled water after thawing and forced through a Pasteur pipette 20 to 40 times. The washing water was exchanged 3 times. Subsequently the isolated mesoglea was transported to a dry Petri dish with a drop of water and allowed to dry over night at room temperature.

Nano-GISAXS experiments. Nano-GISAXS experiments were performed at the European Synchrotron Radiation Facility (ESRF) beamline ID13 (Grenoble, France). Mesogleas were isolated 2-3 days before experiments and deposited on a 100 nm thick silicon nitride window surrounded by a silicon frame (SPI supplier, United States). Experiments were performed on dehydrated samples and at ambient temperature and pressure. Mesogleas were probed with a 200 nm beam with a wavelength of 0.81 Å (15.3 keV) and at an incident angle of 0.46°. Data was collected with a 2D detector (Maxipix, ESRF, France) (48). Silver behenate was used for calibration.

Nano-indentation experiments. Nano-indentation was performed utilizing a JPK-NanoWizard3 atomic force microscope (JPK, Germany) mounted on a Zeiss Axiovert 200 microscope (Zeiss, Germany). Silicon nitride Cantilevers with a nominal spring constant of 10 mN/m and tip-radius of 20 nm were used (MLCT-Probes purchased from Bruker, United States). Indentation experiments were carried out in 150 mM sodium chloride solution. The spring constant of each cantilever was determined prior to measurements using the thermal noise method. A total number of $n = 38$ Hydras out of a daily fed synchronized culture were examined. Sampled Hydras were between 0 and 10 days old and bore no more than 3 buds. Depending on the size, each mesoglea was indented at 7-37 different positions along the body column. Mesoglea was indented with a speed of 2-6 µm/s and up to a cantilever deflection of 0.8 V relative to the baseline. At each position along the Hydra body axis 4 points with a distance of 5 µm were indented. Each spot was indented two times. Subsequent measurements at the same spot with a standard deviation larger than 10% were discarded. Local elastic moduli at each position on measoglea were determined by averaging over the 8 measurements. Data points with standard deviation larger than 40% were discarded. The relative measurement position was determined using ImageJ (49).

Nano-indentation data analysis. The Young's modulus was

extracted using:

$$z = z_0 + d\text{-}d_0\text{-}\sqrt{\frac{2\cdot(1-\nu^2)\cdot k\cdot(d\text{-}d_0)}{1.4906\cdot E\cdot\tan\phi}} \qquad (1)$$

(50) and by plugging the Bilodeau model for a pyramidal tip (25) into the equation. z corresponds to Piezo-position, d to cantilever deflection, z_0 and d_0 correspond to piezo-position and deflection of cantilever at the first tip-sample contact, respectively. E represents the sample's Young's modulus, φ corresponds the half opening angle of the tip, k gives the spring constant of the cantilever and μ corresponds to Poisson's ratio. The Poisson's ratio was set to μ = 0.5. A modification of algorithm used by Lin et al. (27) and Dimitriadis et al. (26) was applied.

For the evaluation of the Young's modulus a so-called "marching range" ($s_{marching}$) was defined around the onset point as described in supporting information. The marching range is assumed to include the point of first tip-sample contact. Hence, the model is moved over the contact point candidates in $s_{marching}$ as follows.

For each contact point candidate:

$$(z_0^*, d_0^*) \in s_{marching} \qquad (2)$$

the model in equation 1 was fitted to the region of the dataset defined by:

$$\{(z,d) \in data | z < z_0^* \wedge d < (d_0^* + d_e)\} \qquad (3)$$

where z and z_0^* correspond to the piezo position of data points and contact point candidate chosen from marching range, respectively. d and d_0^* represent the corresponding cantilever deflections. d_e determines the end of the fitting range and was set to 0.5 V in this study. The fits were compared with regard to their mean sum of square residuals. The Young's modulus was extracted from the best fit.

SILAC Hydra. SILAC Hydra were produced as described earlier (28)

Mass spectrometry. Proteome samples were prepared as described in SI Material and Methods and analyzed in three biological replicates on an LTQ-Orbitrap XL mass spectrometer coupled to a nanoAcquity ultra performance LC system. The reverse phase-LC system consists of a 5 µm SymmetryC18 pre column and a 1.7 µm BEH130 C18 analytical column. Peptide mixtures were loaded on the pre column at a flow rate of 7 µL/min and were then eluted with a linear gradient at a flow rate of 0.4 µL/min. The mass spectrometer was operated in the data-dependent mode to automatically measure MS and MS2. LTQ-Orbitrap XL was set to acquire a full scan at 60000 resolution at 400 m/z from 350 to 1500 m/z and simultaneously fragment the top 6 peptide ions in each cycle in the LTQ. The selected ions were excluded from MS/MS for 35 seconds.

Acknowledgements

This work was supported by the German Science Foundation (DFG, CRC 873, A1 to TWH and B7 to MT). M.V. thanks DFG for fellowships (GRK1114 and EcTop2). We thank H. Watanabe for stimulating discussions and M. Sontag González and F. Gebert for experimental assistance.

References

1. Bonnans C, Chou J, & Werb Z (2014) Remodelling the extracellular matrix in development and disease. *Nat. Rev. Mol. Cell Biol.* 15(12):786-801.
2. Ivanovska IL, Shin J-W, Swift J, & Discher DE (2015) Stem cell mechanobiology: diverse lessons from bone marrow. *Trends Cell Biol.* 25(9):523-532.
3. Cameron AR, Frith JE, & Cooper-White JJ (2011) The influence of substrate creep on mesenchymal stem cell behaviour and phenotype. *Biomaterials* 32(26):5979-5993.
4. Navaro Y, *et al.* (2015) Matrix stiffness determines the fate of nucleus pulposus–derived stem cells. *Biomaterials* 49:68-76.
5. Vincent LG, Choi YS, Alonso-Latorre B, Álamo JCd, & Engler AJ (2013) Mesenchymal stem cell durotaxis depends on substrate stiffness gradient strength. *Biotechnology Journal* 8(4):472-484.
6. Booth AJ, *et al.* (2012) Acellular Normal and Fibrotic Human Lung Matrices as a Culture System for In Vitro Investigation. *Am. J. Respir. Crit. Care Med.* 186(9):866-876.
7. Frank V, *et al.* (2016) Frequent mechanical stress suppresses proliferation of mesenchymal stem cells from human bone marrow without loss of multipotency. *Sci. Rep.* 6:24264.
8. Engler AJ, Sen S, Sweeney HL, & Discher DE (2006) Matrix elasticity directs stem cell lineage specification. *Cell* 126(4):677-689.
9. Arulmoli J, *et al.* (2015) Static stretch affects neural stem cell differentiation in an extracellular matrix-dependent manner. *Sci. Rep.* 5:8499.
10. Bosch TCG (2009) Hydra and the evolution of stem cells. *Bioessays* 31(4):478-486.
11. Sarras MP (2012) Components, structure, biogenesis and function of the Hydra extracellular matrix in regeneration, pattern formation and cell differentiation. *Int. J. Dev. Biol.* 56(6-8):567-576.
12. Shimizu H, *et al.* (2008) The extracellular matrix of hydra is a porous sheet and contains type IV collagen. *Zoology* 111(5):410-418.
13. Deutzmann R, *et al.* (2000) Molecular, biochemical and functional analysis of a novel and developmentally important fibrillar collagen

(Hcol-I) in hydra. *Development* 127(21):4669-4680.
14. Sarras Jr MP, *et al.* (1991) Extracellular matrix (mesoglea) of Hydra vulgaris: I. Isolation and characterization. *Dev. Biol.* 148(2):481-494.
15. Leontovich AA, Zhang J, Shimokawa K, Nagase H, & Sarras MP (2000) A novel hydra matrix metalloproteinase (HMMP) functions in extracellular matrix degradation, morphogenesis and the maintenance of differentiated cells in the foot process. *Development* 127(4):907-920.
16. Shimizu H, *et al.* (2002) Epithelial morphogenesis in hydra requires de novo expression of extracellular matrix components and matrix metalloproteinases. *Development* 129(6):1521-1532.
17. Zhang X, Hudson BG, & Sarras Jr MP (1994) Hydra Cell Aggregate Development Is Blocked by Selective Fragments of Fibronectin and Type IV Collagen. *Dev. Biol.* 164(1):10-23.
18. Hausman RE & Burnett AL (1970) The mesoglea of hydra. III. Fiber system changes in morphogenesis. *J. Exp. Zool.* 173(2):175-185.
19. Burnett AL & Hausman RE (1969) Mesoglea of Hydra .2. Possible Role in Morphogenesis. *J. Exp. Zool.* 171(1):15-23.
20. Aufschnaiter R, *et al.* (2011) In vivo imaging of basement membrane movement: ECM patterning shapes Hydra polyps. *J. Cell Sci.* 124(23):4027-4038.
21. Gambini C, Abou B, Ponton A, & Cornelissen Annemiek JM (2012) Micro- and Macrorheology of Jellyfish Extracellular Matrix. *Biophys. J.* 102(1):1-9.
22. Brusca RC, Moore W, & Shuster SM (2016) *Phylum Cnidaria: Anemones, Corals, Jellyfish, and Their Kin. Invertebrates, (Sinauer Associates, Inc.), pp 265-326.*
23. Wess TJ, Hammersley A, Wess L, & Miller A (1995) Type I collagen packing, conformation of the triclinic unit cell. *J. Mol. Biol.* 248(2):487-493.
24. Davis L & Haynes J (1968) An ultrastructural examination of the mesoglea of Hydra. *Z. Zellforsch. Mikrosk. Anat.* 92(2):149-158.
25. Bilodeau GG (1992) Regular Pyramid Punch Problem. *Journal of Applied Mechanics* 59(3):519-523.
26. Dimitriadis EK, Horkay F, Maresca J, Kachar B, & Chadwick RS (2002) Determination of elastic moduli of thin layers of soft material using the atomic force microscope. *Biophys. J.* 82(5):2798-2810.
27. Lin DC, Dimitriadis EK, & Horkay F (2006) Robust Strategies for Automated AFM Force Curve Analysis—I. Non-adhesive Indentation of Soft, Inhomogeneous Materials. *J. Biomech. Eng.* 129(3):430-440.
28. Petersen HO, *et al.* (2015) A Comprehensive Transcriptomic and Proteomic Analysis of Hydra Head Regeneration. *Mol. Biol. Evol.* 32(8):1928-1947.
29. Augustin R, *et al.* (2006) Dickkopf related genes are components of the positional value gradient in Hydra. *Dev Biol*. 296(1):62-70.
30. Guder C, *et al.* (2006) An ancient Wnt-Dickkopf antagonism in Hydra. *Development* 133(5):901-911.
31. Holstein TW (2012) The Evolution of the Wnt Pathway. *Cold Spring Harb. Perspect. Biol.* 4(7):a007922
32. Hobmayer B, *et al.* (2000) WNT signalling molecules act in axis formation in the diploblastic metazoan Hydra. *Nature (London)* 407(6801):186-189.
33. Lyu J & Joo CK (2005) Wnt-7a up-regulates matrix metalloproteinase-12 expression and promotes cell proliferation in corneal epithelial cells during wound healing. *J Biol Chem* 280(22):21653-21660.
34. Wu B, Crampton SP, & Hughes CC (2007) Wnt signaling induces matrix metalloproteinase expression and regulates T cell transmigration. *Immunity* 26(2):227-239.
35. Kessenbrock K, *et al.* (2013) A role for matrix metalloproteinases in regulating mammary stem cell function via the Wnt signaling pathway. *Cell Stem Cell* 13(3):300-313.
36. Egea V, *et al.* (2012) Tissue inhibitor of metalloproteinase-1 (TIMP-1) regulates mesenchymal stem cells through let-7f microRNA and Wnt/beta-catenin signaling. *Proc Natl Acad Sci U S A* 109(6):E309-316.
37. Broun M, Gee L, Reinhardt B, & Bode HR (2005) Formation of the head organizer in hydra involves the canonical Wnt pathway. *Development* 132(12):2907-2916.
38. Nakamura Y, Tsiairis CD, Özbek S, & Holstein TW (2011) Autoregulatory and repressive inputs localize Hydra Wnt3 to the head organizer. *Proc. Natl. Acad. Sci. U. S. A.* 108(22):9137-9142.
39. Yoshikawa HY, *et al.* (2011) Quantitative Evaluation of Mechanosensing of Cells on Dynamically Tunable Hydrogels. *J. Am. Chem. Soc.* 133(5):1367-1374.
40. Watanabe H, Hoang VT, Mättner R, & Holstein TW (2009) Immortality and the base of multicellular life: Lessons from cnidarian stem cells. *Semin. Cell Dev. Biol.* 20(9):1114-1125.
41. Reilly GC & Engler AJ (2010) Intrinsic extracellular matrix properties regulate stem cell differentiation. *Journal of Biomechanics* 43(1):55-62.

42. Roth SV, *et al.* (2007) In situ observation of nanoparticle ordering at the air-water-substrate boundary in colloidal solutions using x-ray nanobeams. *Applied Physics Letters* 91(9):091915.
43. Hulmes DJS & Miller A (1979) Quasi-hexagonal molecular packing in collagen fibrils. *Nature* 282(5741):878-880.
44. Orgel JPRO, Irving TC, Miller A, & Wess TJ (2006) Microfibrillar structure of type I collagen in situ. *Proc. Natl. Acad. Sci. U. S. A.* 103(24):9001-9005.
45. Holstein TW, Watanabe H, & Ozbek S (2011) Signaling pathways and axis formation in the lower metazoa. *Curr Top Dev Biol* 97:137-177.
46. Reinhardt B, Broun M, Blitz IL, & Bode HR (2004) HyBMP5-8b, a BMP5-8 orthologue, acts during axial patterning and tentacle formation in hydra. *Dev. Biol.* 267(1):43-59.
47. Lenhoff HM & Brown RD (1970) Mass culture of hydra: an improved method and its application to other aquatic invertebrates. *Lab. Anim.* 4(1):139-154.
48. Ponchut C, *et al.* (2011) MAXIPIX, a fast readout photon-counting X-ray area detector for synchrotron applications. *Journal of Instrumentation* 6(01):C01069.
49. Schneider CA, Rasband WS, & Eliceiri KW (2012) NIH Image to ImageJ: 25 years of image analysis. *Nat Meth* 9(7):671-675.
50. Domke J & Radmacher M (1998) Measuring the Elastic Properties of Thin Polymer Films with the Atomic Force Microscope. *Langmuir* 14(12):3320-3325.